European Congress on Computational Methods
in Applied Sciences and Engineering (ECCOMAS 2012)
J. Eberhardsteiner et.al. (eds.)
Vienna, Austria, September 10-14, 2012

INVERSION OF SEISMIC REFLECTION DATA THROUGH FOCUSING

W.A. Mulder

[1]Shell Global Solutions International and Delft University of Technology
PO Box 60, 2280 AB Rijswijk, The Netherlands

Keywords: seismic inversion, acoustics, imaging, subsurface characterization

Abstract. *Since most of the easy hydrocarbon reservoirs have been found, accurate subsurface imaging for oil and gas exploration and production is crucial. Seismic data can provide a band-limited reconstruction of impedance contrasts between different rock formations as well as a subsurface velocity model. Current compute power allows for the use of the full acoustic wave equation for seismic imaging and processing. Least-squares data fitting is an obvious approach but may provide the wrong answer because of local minima in the cost function caused by the absence of low frequencies in the data. An alternative formulation is based on extended images that invokes action at distance to make up for errors in the estimated subsurface velocity model. The action at distance is accomplished by a subsurface shift and the correct model should focus amplitudes at zero shift. The related cost function penalizes image amplitudes at non-zero shift. It has a large basin of attraction but loses its sharpness closer to the minimum. A new formulation is proposed – motivated by high-frequency asymptotic analysis – that provides better results on synthetic and real seismic data and is less sensitive to imaging artifacts.*

1 INTRODUCTION

Since most of the easy hydrocarbon reservoirs have been found, accurate subsurface imaging for oil and gas exploration and production is crucial. Among electro-magnetics, gravity, and wave propagation, seismic data provide the best resolution. The exponential growth in compute power allows for the use of the full wave equation in seismic data processing and imaging. A similar but slower exponential growth of seismic data volumes requires automatic algorithms for seismic imaging and inversion. Unfortunately, straightforward least-squares data fitting with the aim to find a subsurface model that best explains the data suffers from local minima in the cost function. To avoid convergence to the wrong solution, an initial velocity model is required that already provides a data fit with a timing error of less than half the dominant wavelength, thereby increasing the amount of human effort.

An alternative method is based on focusing of the subsurface image. The usual approach to seismic imaging involves least-squares inversion of the primary reflection data subject to the Born approximation of the acoustic wave equation in a velocity model constructed by other means. The gradient of the least-squares cost functional represents a subsurface image, called a migration image by geophysicists. The velocity model for the Born modelling is kept fixed and if it is wrong, the positioning of reflectors, which are band-limited reconstructions of the impedance contrasts, will be wrong as well or the reflectors may even not show up at all.

The subsurface image can be extended by introducing an additional shift parameter. This shift can be interpreted as action at distance and makes up for velocity errors, hence travel time errors [13, 21, 14, 23, 25]. The extended subsurface image may then focus at non-zero shift. By constructing a functional that penalizes non-zero shift, a proper velocity model can be found.

Initial tests have shown that this approach works well if the data have been carefully processed to remove multiple reflections. Still, once the iterations move closer to the correct model, the method starts to deteriorate. This suggests that the approach has a much wider basin of attraction than least-squares fitting, but is not sharp enough when the minimum is approached. An alternative formulation is therefore proposed, maximizing the amplitudes of the extended image around zero shift.

2 METHOD

The explain migration velocity analysis with shifts at depth, the term 'migration', common in seismic processing, is explained in terms of the gradient of the first iteration of a least-squares cost functional that measures the difference between modelled and observed data for a given subsurface velocity model. Migration velocity analysis attempts to improve the focusing of that image by updating the velocity model via an extended migration image. The latter involves spatial shifts at depth that can be interpreted as action at distance to compensate for velocity errors. The correct velocity model should then be obtained for optimal focusing at zero spatial shift.

2.1 Least-squares inversion

The constant-density acoustic wave equation in the frequency domain is

$$L(m)p = f_s, \quad L = -\omega^2 m - \Delta, \tag{1}$$

with $\omega = 2\pi f$ the angular frequency at frequency f, $p(\mathbf{x},\omega)$ the pressure, and $f_s(\mathbf{x},\omega)$ a source term. The model parameters are $m = c^{-2}$ with $c(\mathbf{x})$ the wave speed as a function of position. Typically, the source term $f_s(\mathbf{x},\omega) = w(\omega)\delta(\mathbf{x}-\mathbf{x}_s)$ with source signature or wavelet $w(\omega)$ and a delta function centred at source position $\mathbf{x}_s$ for shot number s.

Inversion of Eq. (1) with least-squares data fitting requires minimization of the cost functional

$$J^{\mathrm{LS}} = \tfrac{1}{2}\sum_{\omega}\sum_{s}\sum_{r(s)} |S_{r(s)}p_s - p^{\mathrm{obs}}_{r(s)}|^2, \tag{2}$$

where the summation runs over the discrete set of frequencies, shots s, and receivers $r(s)$. The restriction operator $S_{r(s)}$ samples the modelled wavefield $p_s(\mathbf{x},\omega)$ for shot number s at location $\mathbf{x}_{r(s)}$ for a given velocity model $c(\mathbf{x})$. The result should match the observed data $p^{\mathrm{obs}}_{r(s)}$. In principle, the velocity model $c(\mathbf{x})$ can be found my minimization of J^{LS} with respect to $c(\mathbf{x})$. In practice, this approach often fails because of absent or unreliable low frequencies in the data, causing a gradient-based optimization algorithm to end up in the nearest local minimum rather than the global minimum.

A major simplification of the inverse problem is its linearization with respect to the model. The assumption is that the large-scale trend of the velocity model can be found by some method and that only small-scale perturbations have to be reconstructed from the data. The governing equation is the Born approximation of the wave equation. The model is split into a smooth background model, $m_0 = c_0^{-2}$ and an oscillatory part $m_1 = c_1^{-2}$, according to $m = c^{-2} = m_0 + m_1$, the idea being that m_0 does not produce reflected waves in the seismic frequency band, typically between 10 and 100 Hz. The wavefield can be split accordingly into $p = p_0 + p_1$. In the Born approximation, the cross-term with $m_1 p_1$ is ignored, leading to the system

$$L_0 p_0 = f_s, \quad L_0 p_1 = \omega^2 m_1 p_0, \tag{3}$$

with an operator $L_0 = -\omega^2 m_0 - \Delta$. Minimization of Eq. (2) for the 'reflectivity' m_1 is now a linear inverse problem that is readily solved with a preconditioned conjugate-gradient method [18, 16]. With proper preconditioning [20, 16], one conjugate-gradient iteration may even suffice and we obtain a procedure that is called migration by exploration geophysicists. A necessity for migration to produce good results is an accurate background velocity model and data that have been preprocessed such that they only contain primary reflections. Direct waves, multiply scattered waves, diving waves, etc. should be filtered out.

The subsurface image obtained by migration is just the scaled gradient of the first iteration of least-squares data fitting subject to either the original wave equation or its Born approximation. Only at the next iteration, these algorithms start to differ. Modelling with the wave equation leads to a highly nonlinear minimization problem plagued by local minima. This approach is called full waveform inversion and requires a good initial velocity model to obtain an acceptable result. With the Born approximation, the linearized inverse problem is easier to solve but it requires the correct background velocity model as input.

The gradient of the functional J^{LS} with respect to the model, $m(\mathbf{x})$, is [10, e.g.]

$$\nabla_m J = \mathrm{Re}\sum_{\omega}\sum_{s}\left(\omega^2 p_s\right)^* q_s, \quad \text{with } L^{\mathsf{H}} q_s = \sum_{r(s)} S^{\mathsf{T}}_{r(s)}\left[S_{r(s)}p_s - p^{\mathrm{obs}}_{r(s)}\right]. \tag{4}$$

The asterisk denotes the complex conjugate, the superscript $(\cdot)^{\mathsf{T}}$ the transpose, and the superscript $(\cdot)^{\mathsf{H}}$ the conjugate transpose. Here, $q(\mathbf{x},\omega)$ solves the 'reverse-time' problem with the receivers acting as sources. For migration, the data residual $S_{r(s)}p_s - p^{\rm obs}_{r(s)}$ reduces to $-p^{\rm obs}_{1,r(s)}$ in the first iteration, where the reflected data in the reflection-free background model are zero and where $p^{\rm obs}_{1,r(s)}$ denote data that have been processed to remove all but the primary reflections. Usually, that goal cannot be fully reached but current processing algorithms can take us a long way. With linearized inversion, subject to Eq. (3), we have a gradient

$$\nabla_{m_1} J = \mathrm{Re} \sum_{\omega} \sum_{s} (\omega^2 p_{0,s})^* q_{1,s}, \quad \text{with } L^{\mathsf{H}} q_{1,s} = \sum_{r(s)} S^{\mathsf{T}}_{r(s)} \left[S_{r(s)} p_{1,s} - p^{\rm obs}_{1,r(s)} \right]. \tag{5}$$

The iterative solution of this problem is called least-squares migration. Classic migration methods perform only a single step, using suitable migration weights that are a diagonal approximation of the hessian of the inverse problem [20, 16].

2.2 Migration velocity analysis

Both in the nonlinear and linearized case, the construction of an initial or background velocity model is a challenge. The classic ray-based approach to velocity analysis uses the redundancy in the data to improve the velocity model. The subsurface should be the same for different subsets of the data. One compares migration images for small and large offsets, offset being defined as the source-receiver distances, or for small and large subsurface scattering angles. If these images are different, the velocity should be changed. Differential semblance optimization attempts to accomplish velocity updating towards the correct model in an automatic way [26, 17, 27].

With rays, an approximation of the Green function is computed for each shot and receiver separately. With wave-equation methods, the cost of treating hundreds of receivers separately in 2D, and far more in 3D, is substantial. Therefore, the summation over receivers in Eqs. (4) and (5) is performed before computing q_s, instead of computing the wavefields $q_{r(s)}$ for each receiver separately. Because the information about surface offset or scattering angle is now lost, an alternative parametrization to represent the redundancy in the data is needed. In [13, 21, 1, 2, 24], a spatial shift at depth before correlation is proposed. The physical interpretation of the shift is action at distance. An incorrect velocity model will causes reflected data to be mapped to the wrong position because of errors in the propagation time from the surface to the correct depth. A spatial shift can compensate for these errors, producing a sharp image at non-zero shift. In the correct velocity model, the migration image should be sharpest at zero shift. An obvious alternative is a temporal shift [7, 22, 5, 28], but that option will not be considered here.

In the frequency domain, the extended image for a subsurface shift $\mathbf{h}$ is given by

$$R(\mathbf{x};\mathbf{h}) = \mathrm{Re} \sum_{s,\omega} \omega^2 p^*_s(\mathbf{x} - \tfrac{1}{2}\mathbf{h},\omega) q_s(\mathbf{x} + \tfrac{1}{2}\mathbf{h},\omega). \tag{6}$$

Here, ω is the angular frequency, $p_s(\mathbf{x},\omega)$ is the wavefield generated by source number s at position $\mathbf{x}$, $q_s(\mathbf{x},\omega)$ is the reverse-time wavefield obtained by back-propagating the observed seismic data from all the receivers that recorded shot number s. The asterisk denotes complex conjugation. The usual seismic image is recovered for a zero shift $\mathbf{h}$. A data explosion can be avoided by restricting $\mathbf{h}$ to one of the coordinate directions. In 2D

with horizontal or vertical shifts, the cost function $J = J_x + \gamma J_z$ can be chosen as the weighted sum of

$$J_x = \tfrac{1}{2} \sum_{x,z,h_x} W(x,z)\eta(h_x) \left|\Xi_x R(x,z;h_x,0)\right|^2, \tag{7}$$

and

$$J_z = \tfrac{1}{2} \sum_{x,z,h_z} W(x,z)\eta(h_z) \left|\Xi_z R(x,z;0,h_z)\right|^2. \tag{8}$$

Vertical shifts are required if reflectors have steep dips, that is, are closer to vertical than horizontal [3]. The cost functionals include filters Ξ_x and Ξ_z that should perform several tasks. A first is the removal of low-frequency artifacts in the extended migration image. This can be accomplished by a spatial high-pass filter [16]. Secondly, the filter Ξ_x should remove reflectors with steep dips, whereas the complimentary Ξ_z should remove reflectors that are closer to horizontal. One way to accomplish that in 2D with spatial coordinates x and z is a two-dimensional FFT that that transforms the extended images, $R(x,z;h_x,0)$ and $R(x,z;0,h_z)$, to the wavenumber domain parametrized by wave numbers k_x and k_z. Then, the symbol of Ξ_x can be chosen as $\hat{\Xi}_x(k_x,k_z) = \sqrt{k_z^2/(k_x^2+k_z^2)}$, whereas $\hat{\Xi}_z(k_x,k_z) = \sqrt{k_x^2/(k_x^2+k_z^2)}$ [14]. In [29], a similar, simpler filter was later proposed where Ξ_x represents the spatial derivative in z and Ξ_z in x. These simultaneously perform the dip filtering and emphasize the higher spatial frequencies. However, simple differentiation also may boost noise and imaging artifacts when working with real data.

The spatial weighting function $W(x,z)$ should compensate for amplitude variations between reflectors in the extended image. In this paper, only simple power-law weighting in depth of the form $W(x,z) = \max(0, z-z_{\min})^p$ will be applied. Only J_x will be considered here. Minimization of J_x with a penalty function $\eta(h_x) = h_x^2$ may lead to a focused image [24, 27]. As we will see, this is not the best choice.

Figure 3a shows an example of an extended image in the correct constant velocity model at a fixed lateral position. The details will be described further on. Most of the energy is focused around zero shift. If the velocity is too low, Figure 1a shows that most of the energy occurs at a negative shift, whereas too high a velocity produces a peak at positive shifts in Figure 2a.

3 Asymptotic analysis

To obtain some insight into how reflection data appear in the extended images, asymptotic analysis for the high-frequency limit was carried out for a constant velocity model, using different velocities for the data and for the extended migration image. First, an asymptotic expression for the data generated by a single horizontal reflector is presented. Then, the amplitude behaviour of the extended image is determined along the zero-phase curve were the energy is concentrated. Examples for 2D finite-frequency simulations are included.

3.1 Reflection data for horizontal reflectors

Recall that the principle of stationary phase provides the approximation

$$\int_{-\infty}^{\infty} dz\; a(z) e^{ik\phi(z)} \simeq \sqrt{\frac{\pi}{|k\phi^{(2)}(z_0)|}} a(z_0) e^{ik\phi(z_0)} [1 + i\,\mathrm{sign}(k\phi^{(2)}(z_0))],$$

when k is large [4, e.g.]. The phase $\phi(z)$ is expressed as $\phi(z) \simeq \phi(z_0) + \frac{1}{2}(z-z_0)^2\phi^{(2)}(z_0)$, where the first derivative $\phi^{(1)}(z_0) = 0$ at $z = z_0$. If $\phi^{(1)}$ vanishes at multiple points, $z_{0,j}$, then a summation over j should be performed.

In a constant model with velocity c_0, the solution of the Born approximation of the wave equation in Eq. (3) is

$$p_{1,r(s)} = \int_{-\infty}^{\infty} d\mathbf{x}\ G(\mathbf{x}_s, \mathbf{x}) m_1(\mathbf{x}) G(\mathbf{x}, \mathbf{x}_r),$$

where $G(\mathbf{x}_a, \mathbf{x}_b)$ denotes the Green function for the wave operator L_0 for a delta-function source at $\mathbf{x}_a$ and a receiver at $\mathbf{x}_b$ as well as a delta-function wavelet $w(\omega) = 1$. In the 3D case, the Green function is

$$G^{3\mathrm{D}}(r) = \frac{1}{4\pi r} e^{ikr}, \quad k = \frac{\omega}{c}, \quad r = ||\mathbf{x}_b - \mathbf{x}_a||,$$

with r the distance between $\mathbf{x}_a$ and $\mathbf{x}_b$. In 2D, we have

$$G^{2\mathrm{D}}(r) = \frac{i}{4} H_0^{(1)}(kr) \sim \frac{(1+i)}{4\sqrt{\pi kr}} e^{ikr},$$

where the approximation holds for large kr. It is assumed that the reflectors are all horizontal, as may happen in a simple sedimentary geology. The source and receiver are placed on the surface, at $z = 0$ and the offset, the horizontal distance between source and receiver, is $2\bar{h}$. The sources are then located at $\mathbf{x}_s = (x_m - \bar{h}, 0, 0)$ and the receivers at $\mathbf{x}_s = (x_m + \bar{h}, 0, 0)$. We integrate over y for the 3D case and over the midpoints x_m in both the 2D or 3D case. The stationary-phase result becomes either

$$p^{3\mathrm{D}}(\bar{h}, \omega) \simeq \frac{i\omega w(\omega) c_0}{16\pi} \int_0^{\infty} dz\ z^{-1} m_1(z) e^{2ik_0\bar{r}}, \quad \bar{r} = \sqrt{\bar{h}^2 + z^2}, \quad k_0 = \omega/c_0,$$

or

$$p^{2\mathrm{D}}(\bar{h}, \omega) \simeq \frac{(i-1) w(\omega)}{8} \sqrt{\frac{\omega c_0^3}{2\pi}} \int_0^{\infty} dz\ \frac{\sqrt{\bar{r}}}{z} m_1(z) e^{2ik_0\bar{r}}.$$

Note that $\omega \geq 0$ and that real-valued data in the time domain are obtained with $p(-\omega, \bar{h}) = p^*(\omega, \bar{h})$, $\omega > 0$.

In the following, only a delta-function reflector at $z = z_0$ will be considered, representing a single horizontal reflector. Then,

$$p(\bar{h}, \omega) \simeq w(\omega) A_0 e^{2ik_0 r_0}, \quad A_0^{2\mathrm{D}} = \frac{(i-1)}{8z_0} \sqrt{\frac{\omega c_0^3 r_0}{2\pi}}, \quad A_0^{3\mathrm{D}} = \frac{i\omega c_0}{16\pi z_0}, \quad r_0 = \sqrt{\bar{h}^2 + z_0^2}.$$

3.2 Extended image

If the data are shot on a seismic line in the plane $y = 0$, the extended image in Eq. (6) in that plane becomes

$$R(x, z; 2\bar{h}_x, 0) = \mathrm{Re} \int_{-\infty}^{\infty} d\omega\ \omega^2 \mathcal{F}(\omega) \int d\bar{h} \int_{-\infty}^{\infty} dx_m\ p^*(x - \bar{h}_x, z, \omega) q_{\bar{h}}(x + \bar{h}_x, z, \omega), \quad (9)$$

where the variable y has been dropped. The wavelet and additional data filters are included as $\mathcal{F}(\omega)$. In this expression, the wavefields p and q are determined by the Green

functions for a different model with constant velocity c, but the data fed into q correspond to a velocity c_0. We have replaced $q(\cdot)$ by $\int d\bar{h}\, q_{\bar{h}}(\cdot)$ corresponding to observed data at half-offset $\bar{h}$, that is, each receiver is treated separately in the analysis. The integration interval for $\bar{h}$ depends on the acquisition geometry. With a seismic line on land, we typically have $\bar{h}_{\min} < 0 < \bar{h}_{\max}$. For a marine survey with a towed receiver cable, we can consider $\bar{h} \in [\bar{h}_{\min}, \bar{h}_{\max}] \subset (0, \infty)$, which will be assumed to be case in what follows.

The wavefields in Eq. (9) are given by

$$p^*(x - \bar{h}_x, z, \omega) = G^*[c](r_1), \quad r_1 = \sqrt{\{(x - \bar{h}_x) - (x_m - \bar{h})\}^2 + z^2},$$

and

$$q_{\bar{h}}(x + \bar{h}_x, z, \omega) = G^*[c](r_2) p[c_0](\bar{h}, \omega), \quad r_2 = \sqrt{\{(x + \bar{h}_x) - (x_m + \bar{h})\}^2 + z^2},$$

where the dependence on c and c_0 has been made explicit with the square brackets. Then

$$R(x, z; 2\bar{h}_x, 0) = \mathrm{Re} \int_{-\infty}^{\infty} d\omega\ \mathcal{F}(\omega) \int d\bar{h} \int_{-\infty}^{\infty} dx_m\ A_1 e^{i\psi_0},$$

with amplitude

$$A_1^{\mathrm{2D}} = \mathcal{F}(\omega)\, \omega^{3/2} \frac{(1+i)c}{64 z_0} \sqrt{\frac{c_0^3 r_0}{2\pi^3 r_1 r_2}}, \quad A_1^{\mathrm{3D}} = \mathcal{F}(\omega)\, \omega^3 \frac{i c_0}{256 \pi^3 z_0 r_1 r_2},$$

and phase

$$\psi_0 = \omega \left(\frac{2r_0}{c_0} - \frac{r_1 + r_2}{c} \right).$$

Stationarity of the phase requires zero derivatives with respect to half-offset $\bar{h}$ and midpoint x_m, which happens at

$$x_m = x, \quad \bar{h}_x = \bar{h} \left(1 - \gamma^2 \frac{z}{z_c} \right),$$

where $\gamma \coloneqq c/c_0$, $\beta \coloneqq \gamma^2 - 1$, and $z_c \coloneqq \gamma \sqrt{z_0^2 - \beta \bar{h}^2}$. Note that $\bar{h}$ is defined implicitly and that we assume $z_0 \geq \bar{h}\sqrt{\beta}$ if $\beta \geq 0$ At the stationary point, the phase is $-\omega \frac{2r_0(z - z_c)}{c_0 z_c}$. Its hessian at that point is diagonal with

$$\frac{\partial^2 \psi_0}{\partial \bar{h}^2} = \frac{2\omega(\gamma^4 z z_0^2 - z_c^3)}{c_0 \gamma^4 r_0^3 z} = \frac{2\omega z_0^2 (z - z_1)}{c_0 r_0^3 z}, \quad \frac{\partial^2 \psi_0}{\partial x_m^2} = \frac{-2\omega z_c^3}{c_0 \gamma^4 r_0^3 z} < 0,$$

where $z_1 \coloneqq z_c^3/(\gamma^4 z_0^2)$. The amplitudes reduce to

$$A_1^{\mathrm{2D}} = \mathcal{F}(\omega) \frac{(1+i) z_c}{64 z z_0} \sqrt{\frac{\omega^3 c_0^5}{2\pi^3 r_0}}, \quad A_1^{\mathrm{3D}} = \mathcal{F}(\omega) \frac{i \omega^3 z_c^2 c_0}{256 \gamma^2 \pi^3 z_0 z^2 r_0^2}.$$

After integration over x_m and $\bar{h}$, the phase is $\psi_1 = -\omega \frac{2r_0(z - z_c)}{c_0 z_c}$, as mentioned above, and the amplitudes become

$$A_2^{\mathrm{2D}} = \mathcal{F}(\omega) \frac{[1 + i\,\mathrm{sign}(z - z_1)] z_c}{64 z_0^3} \sqrt{\frac{\omega c_0^7 r_0^5}{2\pi z_1 |z - z_1|}},$$

$$A_2^{3D} = \mathcal{F}(\omega)\frac{[1+i\,\mathrm{sign}(z-z_1)](1+i)r_0 z_c^2 c_0^2\omega^2}{512\gamma^2\pi^2 z z_0^3\sqrt{z_1|z-z_1|}}.$$

For the last step, we have to evaluate

$$A = 2\mathrm{Re}\int_0^\infty d\omega\, A_2 e^{i\omega\phi_1}, \quad \phi_1 = \psi_1/\omega = -\frac{2r_0(z-z_c)}{c_0 z_c}.$$

For simplicity, the frequency dependence of the amplitudes is removed by letting $\mathcal{F}(\omega) = \omega^{-1/2}$ in the 2-D and $\mathcal{F}(\omega) = \sqrt{2}/(\omega^2(1+i)) = \omega^{-2}e^{-i\pi/4}$ in the 3-D case. For the integration, we can use $A = \int_0^{\omega_{\max}} d\omega\,[A_2 e^{i\omega\phi_1} + A_2^* e^{-i\omega\phi_1}]$ and

$$\lim_{\omega_{\max}\to\infty}\frac{\sin(\omega_{\max}\phi_1)}{\phi_1} = \pi\delta(\phi_1) = \pi\frac{\delta(z-z_{c,0})}{\left|\frac{d\phi_1}{dz}(z_{c,0})\right|}.$$

To evaluate $d\phi_1/dz$, we can determine $d\bar{h}/dz$ from $\bar{h}_x = \bar{h}\left(1-\gamma^2\frac{z}{z_c}\right)$ and $z_c = \gamma\sqrt{z_0^2-\beta\bar{h}^2}$. Then,

$$\frac{d\phi_1}{dz}(z_{c,0}) = -\frac{2z_{c,0}}{\gamma^2 c_0 r_{c,0}}.$$

On the stationary-phase curve, $\bar{h}_x = -\beta\bar{h}$, $z = z_{c,0} \coloneqq \gamma\sqrt{z_0^2-\bar{h}_x^2/\beta}$ and $r_0 = r_{c,0} \coloneqq \sqrt{z_0^2+\bar{h}_x^2/\beta^2}$. If $\beta > 0$, then $\bar{h}_x < 0$ and we should have $(-\bar{h}_x) \le z_0\sqrt{\beta}$ and $\bar{h} \le z_0/\sqrt{\beta}$. The resulting extended image is $R(x,z;\bar{h}_x,0) = A(x,z;\bar{h}_x)\delta(z-z_{c,0})$ with amplitude

$$A^{2D} = \frac{\gamma^5}{128 z_0 z_{c,0}^2}\sqrt{\frac{2\pi c_0^9 r_{c,0}^5}{|\beta|}}, \quad A^{3D} = \frac{(\gamma c_0)^3 r_{c,0}}{512\pi z_0 z_{c,0}^2}\sqrt{\frac{2}{|\beta|}},$$

in 2D and 3D, respectively.

So far, an infinite acquisition was assumed. If the offset range is truncated at $\bar{h}_m$, the corresponding curve is $z = \sqrt{\gamma^2(\bar{h}_m^2+z_0^2)-(\bar{h}_x-\bar{h}_m)^2}$. Here, $\bar{h}_m$ denotes either the shortest or longest surface half-offset.

3.3 Examples

Extended images were computed for three constant-velocity models in 2 dimensions, with $c < c_0$, $c = c_0$, and $c > c_0$. For the 'observed' data, we considered a velocity $c_0 = 2.0\,\mathrm{km/s}$ and a single horizontal reflector at a depth of 1 km. Shots were placed at zero depth between $x_s = -1500$ and 4500 m at a 25-m interval. Receivers were placed to the right of the shots at offsets between 10 and 4000 m, using a 10-m interval. The data and image were computed with frequencies from 0.5 to 42 Hz with a spacing of 0.5 Hz and with a Ricker wavelet with a 15-Hz peak frequency. The time-domain equivalent of that wavelet is the second derivative of a Gaussian.

Figure 1a shows the extended image at a lateral position $x = 1500\,\mathrm{m}$, in the centre of the problem, as a function of horizontal shift h_x and depth z. Since the velocity is too low, energy at zero shift ends up less deep than it should, less then 1 km. Because on the zero-phase curve, $h_x = 2\bar{h}_x = -2\beta\bar{h} = -\beta h$, and $\beta < 0$ for $c/c_0 < 1$, the energy is concentrated at positive shift h_x as the receivers all have positive offsets $h = 2\bar{h}$. The abrupt truncation of the offsets at their smallest and largest values give rise to the patterns that agree with

the dashed lines. The asymptotic estimate of amplitude along the stationary-phase curve is plotted as a red line in Figure 1b and compared to the numerical finite-frequency result drawn in black. The vertical scale for asymptotic result has been adjusted in an *ad hoc* manner to overlay the black curve. Finite-frequency effects and truncation of the acquisition are probably responsible for the deviations at smaller and larger shifts, but the overall trend is similar.

If the velocity is too high, the results of Figure 2 are obtained. Now, $\beta < 0$ and the energy is mainly concentrated at negative shifts h_x for positive surface offsets h.

Figure 3a shows the extended image for the correct velocity model. Now, the image peaks at zero shift and at the correct depth of 1 km. However, the artifacts due to the shortest and longest offset persist. With tapering, we obtain the result in Figure 3b. The recorded data were multiplied by the window function $w_r = [4\xi(1-\xi)]^{p_w}$, with $\xi = j/(n_r+1)$ for $j = 1, \ldots, n_r$ corresponding to offsets $h_j = h_{\min} + (j-1)\Delta h$, with $h_{\min} = \Delta h = 10\,\text{m}$ as mentioned earlier. For the power, we used $p_w = 1$. On top of that, a shot taper w_s was applied that was a linear ramp over 10% of the full shot range at the beginning and at the end. These tapers reduce the effect of the artifacts but do not fully remove them.

3.4 Weighting

As mentioned before, focusing at zero shift can be accomplished by penalizing non-zero shift, typically by choosing $\eta(h_x) = \eta_1(h_x) = h_x^2$ in the expression (7) for J_x. The asymptotic analysis, however, suggest that this may not be the best choice. Even with tapers, the energy is smeared out over two curves, in particular for the largest offset, as evident in Figure 3b. With the one-sided acquisition, this curve is not symmetric and this may cause problems. In the wrong model, the peak along the stationary-phase curve occurs at the maximum surface offset. As can be seen in Figures 1a and 2, the corresponding point is located at a depth that can be far away from the true depth of the reflector. The corresponding contribution to the gradient of the cost functional with respect to the velocity model may have large contributions at depths were other reflectors (not present in the current example) may have been focused correctly, thereby damaging other parts of the model.

A better approach would be to concentrate on the part of the curve that is closer to zero subsurface shift. We can instead *maximize* the energy inside the region close to zero offset with, for instance, a weighting function $\eta_2(h_x) = [1 + (h_x/\ell_x)^2]^{-p}$ that decays with h_x for $p > 0$. The length ℓ_x is related to the finite-frequency width of the peak at zero shift in the correct model.

4 Results

4.1 Velocity scan

To test the performance of the two approaches, one with the original choice $\eta_1(h_x) = h_x^2$ for minimization of J_x and one with the new weighting function $\eta_2(h_x)$ for maximization, values of the cost functional J_x with either choice were computed in a sequence of constant-velocity models, with c ranging from 1.9 to 2.1 km/s. Figure 4a shows the maximum value of $|R(x, z; h_x, 0)|$ in the extended images at $x = 1.5\,\text{km}$. These imaging include those of the previous figures and include tapers. Note the maximum value occurs for a slightly positive value of the relative velocity error $c/c_0 - 1$. Figure 4b displays the resulting

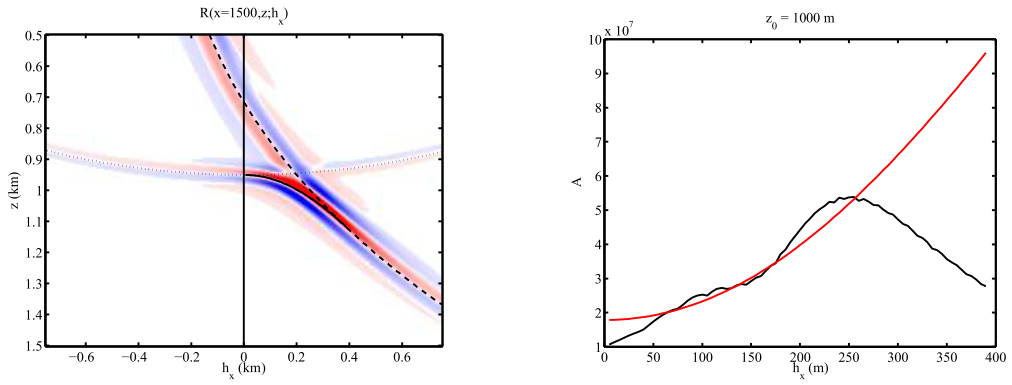

(a) (b)

Figure 1: (a) Extended image at a fixed lateral position x as function of horizontal subsurface offset h_x and depth z for too low a velocity of 1.9 km/s. The dash-dotted line corresponds to the shortest offset, the dashed line to the longest, and the drawn line to the stationary phase curve. The colours show the result of a numerical simulation, with positive values in red and negative in blue. (b) Observed amplitude behaviour (black), measured in a window around the stationary curve, together with the asymptotic result (red), using arbitrary scaling.

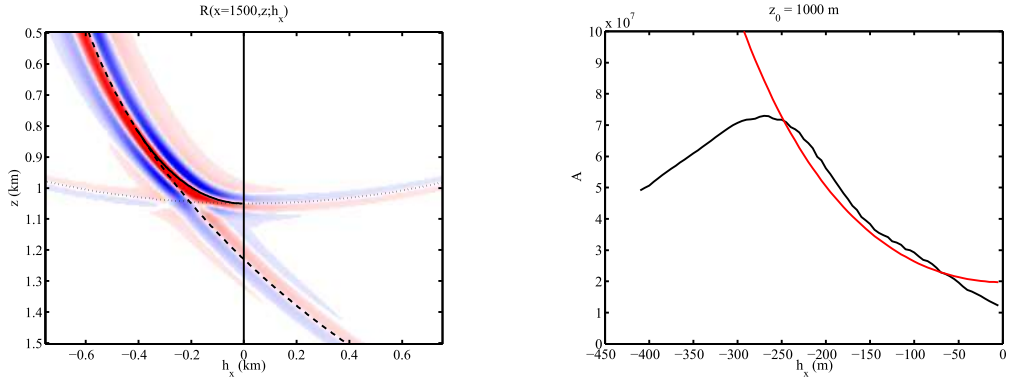

(a) (b)

Figure 2: As Figure 1, but for too high a velocity of 2.1 km/s.

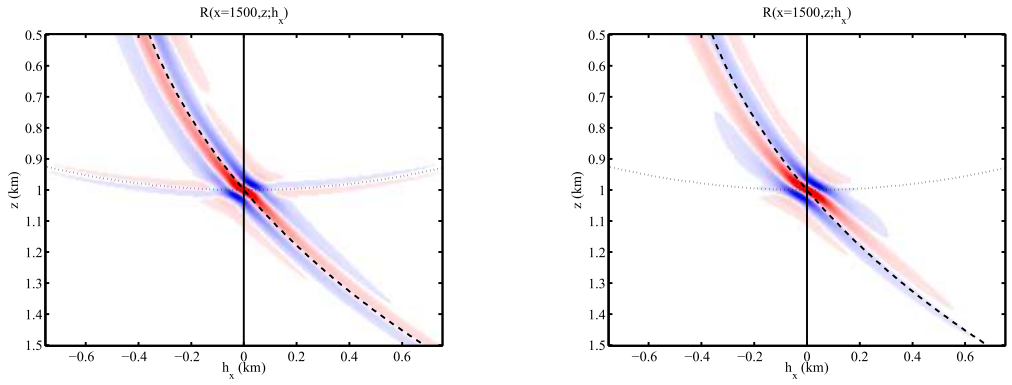

(a) (b)

Figure 3: As Figure 1, but for the correct velocity of 2.0 km/s. Only the extended image is shown without (a) and with (b) tapers.

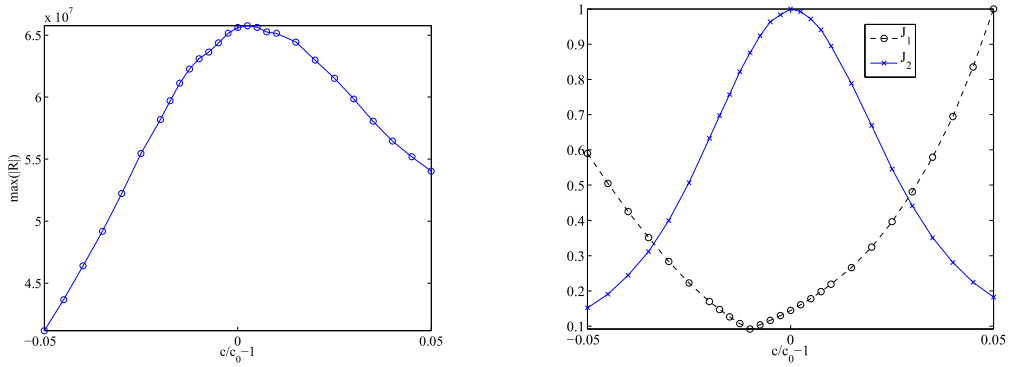

(a) (b)

Figure 4: Scan over a set of constant-velocity models, (a) Observed maximum of $|R(x,z;h_x,0)|$ at $x = 1.5\,\mathrm{km}$ for single-reflector data as a function of the relative velocity error $(c/c_0)-1$. (b) Cost functionals J_1, to be minimized with $\eta_1(h_x)$, and J_2, to be maximized as a function of the velocity error. Note the wrong location of the minimum for J_1.

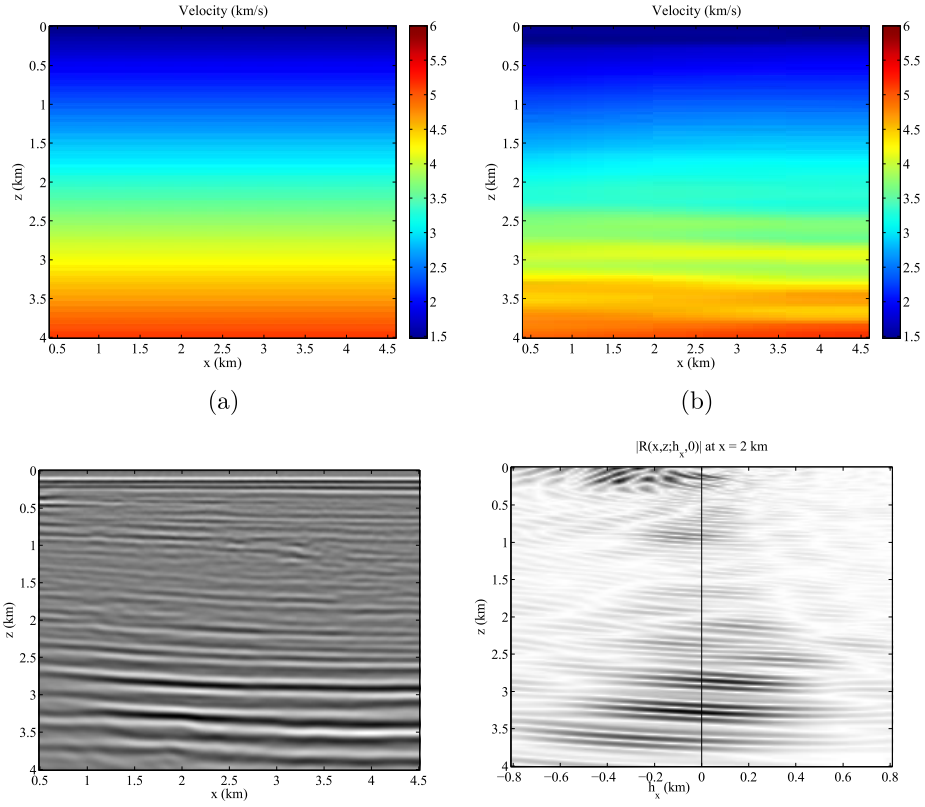

(a) (b)

(c) (d)

Figure 5: (a) Initial model with velocity linear in depth, (b) velocity model after 41 iterations, (c) migration image, (d) amplitudes of the extended image at $x = 14.5\,\mathrm{km}$.

values of the functional, where J_1 is J_x evaluated with η_1 and J_2 with η_2. The minimum of J_1 occurs at the wrong velocity model. The maximum of J_2 has the correct position, demonstrating that this a better choice. The shape of the curve for J_2 can be controlled to some extent by the choice of the parameters p and ℓ_x in the weighting function η_2.

4.2 Real data

The method was applied to a marine data of unspecified origin, with sources and receivers just below the sea water level. Wavefields were computed with a 2-D frequency-domain code [16], using a fourth-order finite-difference discretization [11] of the constant-density acoustic wave equation and a direct solver for the discretized wave operator [8, 15]. The model is represented by linear splines on a grid that is coarser than the one used for modelling. To obtain an initial guess of the model, a one-dimensional optimization based on values of the functional only was carried out over velocity models that are linear in depth, of the form $c(z) = c_0 + \alpha(z - z_0)$, with c_0 set equal to the known water velocity and $z_0 = 1\,\mathrm{m}$. Note that we set $c(z) = c_0$ for $z < 110\,\mathrm{m}$ in the sea water.

Starting from the optimal one-parameter result, shown in Figure 5a, the velocity model in Figure 5b was obtained after 41 iterations with a limited-memory BFGS method [6]. The latter requires the gradient of the functional with respect to the model, which was computed with an adjoint-state approach [12, 9, 19]. The method produced the subsurface image $R(x, z; 0, 0)$ in Figure 5c. The first reflector towards the top of the figure is the sea bottom. The extended image in Figure 5d shows reasonable though not perfect focusing towards zero shift $h_x = 0$.

5 Conclusions

Automatic migration velocity analysis with extended images based on a subsurface shift can be made more robust by maximizing the energy around zero shift rather than minimizing energy at non-zero shift. Asymptotic analysis shows that the energy increases with non-zero shift up to a distance related to the end of the receiver line. Since the maximum energy in the wrong velocity model resides at the wrong depth, the corresponding update of the velocity model may harm the focusing from another reflector at that depth. The proposed alternative suffers less from this behaviour, as it give less weight to larger subsurface shifts.

A marine real-data example demonstrated the usefulness of the method.

REFERENCES

[1] B. Biondi and P. Sava. Wave-equation migration velocity analysis. I. Theory. *Geophysical Prospecting*, 52(6), 593–606, 2004.

[2] B. Biondi and P. Sava. Wave-equation migration velocity analysis. II. Subsalt imaging examples. *Geophysical Prospecting*, 52(6), 607–623, 2004.

[3] B. Biondi and G. Shan. Prestack imaging of overturned reflections by reverse time migration. *SEG Technical Program Expanded Abstracts*, 21(1), 1284–1287, 2002.

[4] N. Bleistein and R. A. Handelsman. *Asymptotic Expansions of Integrals*. Holt, Rinehart and Winston, New York, 1975.

[5] M. P. Brown, J. H. Higginbotham, and R. G. Clapp. Velocity model building with wave equation migration velocity focusing analysis. *SEG Technical Program Expanded Abstracts*, 27(1), 3078–3082, 2008.

[6] R. H. Byrd, P. Lu, J. Nocedal, and C. Zhu. A limited memory algorithm for bound constrained optimization. *SIAM Journal on Scientific Computing*, 16(5), 1190–1208, 1995.

[7] J. Faye and J. Jeannot. Prestack migration velocities from focusing depth analysis. *SEG Expanded Abstracts*, 5, 438–440, 1986.

[8] A. George and J. Liu. *Computer solution of large sparse positive definite systems*. Prentice-Hall, Inc., 1981.

[9] M. B. Giles, M. C. Duta, J. Müller, and N. A. Pierce. Algorithm developments for discrete adjoint methods. *AIAA Journal*, 41(2), 198–205, 2003.

[10] B. Hak and W. A. Mulder. Seismic attenuation imaging with causality. *Geophysical Journal International*, 184(1), 439–451, 2011.

[11] I. Harari and E. Turkel. Accurate finite difference methods for time-harmonic wave propagation. *Journal of Computational Physics*, 119(2), 252–270, 1995.

[12] J. Lions and E. Magenes. *Nonhomogeneous boundary value problems and applications*. Springer Verlag, Berlin, 1972.

[13] S. MacKay and R. Abma. Imaging and velocity analysis with depth-focusing analysis. *Geophysics*, 57(12), 1608–1622, 1992.

[14] W. A. Mulder. Automatic velocity analysis with the two-way wave equation. In *70th EAGE Conference & Exhibition*. Extended Abstracts, P165, European Association of Geoscientists & Engineers, 2008.

[15] W. A. Mulder and R. Plessix. Time- versus frequencyf-domain modelling of seismic wave propagation. In *68th EAGE Conference & Exhibition*. Extended Abstracts, G019, 2002.

[16] W. A. Mulder and R.-É. Plessix. A comparison between one-way and two-way wave-equation migration. *Geophysics*, 69(6), 1491–1504, 2004.

[17] W. A. Mulder and A. P. E. ten Kroode. Automatic velocity analysis by differential semblance optimization. *Geophysics*, 67(4), 1184–1191, 2002.

[18] S. Østmo, W. A. Mulder, and R. Plessix. Finite-difference iterative migration by linearized waveform inversion in the frequency domain. *SEG Technical Program Expanded Abstracts*, 21, 1384–1387, 2002.

[19] R.-E. Plessix. A review of the adjoint-state method for computing the gradient of a functional with geophysical applications. *Geophysical Journal International*, 167(2), 495–503, 2006.

[20] R.-E. Plessix and W. A. Mulder. Frequency-domain finite-difference amplitude-preserving migration. *Geophysical Journal International*, 157(3), 975–987, June 2004.

[21] J. E. Rickett and P. C. Sava. Offset and angle-domain common image-point gathers for shot-profile migration. *Geophysics*, 67(3), 883–889, 2002.

[22] P. Sava and S. Fomel. Time-shift imaging condition in seismic migration. *Geophysics*, 71(6), S200–S217, 2006.

[23] P. Shen, W. W. Symes, and C. C. Stolk. Differential semblance velocity analysis by wave-equation migration. *SEG Expanded Abstracts*, 22, 2132–2135, 2003.

[24] P. Shen, W. W. Symes, and C. C. Stolk. Differential semblance velocity analysis by wave-equation migration. *SEG Technical Program Expanded Abstracts*, 22(1), 2132–2135, 2003.

[25] W. W. Symes. The seismic reflection inverse problem. *Inverse Problems*, 25(12), 123008, 2009.

[26] W. W. Symes and J. J. Carazzone. Velocity inversion by differential semblance optimization. *Geophysics*, 56(5), 654–663, 1991.

[27] W. W. Symes. High frequency asymptotics, differential semblance, and velocity estimation. *SEG Technical Program Expanded Abstracts*, 17(1), 1616–1619, 1998.

[28] T. van Leeuwen and W. A. Mulder. A comparison of seismic velocity inversion methods for layered acoustics. *Inverse Problems*, 26(1), 015008, 2010.

[29] W. W. Weibull. Automatic migration velocity analysis using reverse time migration. In *73rd EAGE Conference & Exhibition*. Extended Abstracts, B012, European Association of Geoscientists & Engineers, 2011.